Stellar Metallicities and Gradients in the Faint M31 Satellites Andromeda XVI and Andromeda XXVIII

Sal Wanying Fu[1] , Daniel R. Weisz[1] , Else Starkenburg[2], Nicolas Martin[3,4] , Michelle L. M. Collins[5] , Alessandro Savino[1] ,
Michael Boylan-Kolchin[6] , Patrick Côté[7] , Andrew E. Dolphin[8,9], Nicolas Longeard[10], Mario L. Mateo[11] ,
Francisco J. Mercado[12] , Nathan R. Sandford[13] , and Evan D. Skillman[14]

[1] Department of Astronomy, University of California, Berkeley, Berkeley, CA 94720, USA; swfu@berkeley.edu
[2] Kapteyn Astronomical Institute, University of Groningen, Postbus 800, 9700 AV, Groningen, The Netherlands
[3] Université de Strasbourg, Observatoire astronomique de Strasbourg, UMR 7550, F-67000 Strasbourg, France
[4] Max-Planck-Institut für Astronomie, Königstuhl 17, D-69117 Heidelberg, Germany
[5] School of Maths and Physics, University of Surrey, Guildford GU2 7XH, UK
[6] Department of Astronomy, The University of Texas at Austin, 2515 Speedway, Stop C1400, Austin, TX 78712-1205, USA
[7] National Research Council of Canada, Herzberg Astronomy and Astrophysics Research Centre, Victoria, BC V9E 2E7, Canada
[8] Raytheon, 1151 E. Hermans Road, Tucson, AZ 85756, USA
[9] Steward Observatory, University of Arizona, 933 North Cherry Avenue, Tucson, AZ 85721-0065, USA
[10] Laboratoire d'astrophysique, École Polytechnique Fédérale de Lausanne (EPFL), Observatoire, 1290 Versoix, Switzerland
[11] Department of Astronomy, University of Michigan, 311 West Hall, 1085 S. University Avenue, Ann Arbor, MI 48109, USA
[12] Department of Physics and Astronomy, Pomona College, Claremont, CA 91711, USA
[13] Department of Astronomy and Astrophysics, University of Toronto, 50 St George Street, Toronto, ON M5S 3H4, Canada
[14] University of Minnesota, Minnesota Institute for Astrophysics, School of Physics and Astronomy, 116 Church Street SE, Minneapolis, MN 55455, USA

Abstract

We present $\sim$300 stellar metallicity measurements in two faint M31 dwarf galaxies, Andromeda XVI ($M_V = -7.5$) and Andromeda XXVIII ($M_V = -8.8$), derived using metallicity-sensitive calcium H and K narrowband Hubble Space Telescope imaging. These are the first individual stellar metallicities in And XVI (95 stars). Our And XXVIII sample (191 stars) is a factor of $\sim$15 increase over literature metallicities. For And XVI, we measure $\langle [\mathrm{Fe/H}] \rangle = -2.17^{+0.05}_{-0.05}$, $\sigma_{[\mathrm{Fe/H}]} = 0.33^{+0.07}_{-0.07}$, and $\nabla_{[\mathrm{Fe/H}]} = -0.23 \pm 0.15$ dex R_e^{-1}. We find that And XVI is more metal-rich than Milky Way ultrafaint dwarf galaxies of similar luminosity, which may be a result of its unusually extended star formation history. For And XXVIII, we measure $\langle [\mathrm{Fe/H}] \rangle = -1.95^{+0.04}_{-0.04}$, $\sigma_{[\mathrm{Fe/H}]} = 0.34^{+0.05}_{-0.05}$, and $\nabla_{[\mathrm{Fe/H}]} = -0.46 \pm 0.10$ dex R_e^{-1}, placing it on the dwarf galaxy mass–metallicity relation. Neither galaxy has a metallicity distribution function (MDF) with an abrupt metal-rich truncation, suggesting that star formation fell off gradually. The stellar metallicity gradient measurements are among the first for faint ($L \lesssim 10^6 L_\odot$) galaxies outside the Milky Way halo. Both galaxies' gradients are consistent with predictions from the FIRE simulations, where an age–gradient strength relationship is the observational consequence of stellar feedback that produces dark matter cores. We include a catalog for community spectroscopic follow-up, including 19 extremely metal-poor ([Fe/H] < -3.0) star candidates, which make up 7% of And XVI's MDF and 6% of And XXVIII's.

Unified Astronomy Thesaurus concepts: Dwarf galaxies (416); HST photometry (756); Local Group (929); Stellar abundances (1577)

Materials only available in the online version of record: machine-readable tables

1. Introduction

Studies of satellite galaxies around the next-nearest spiral galaxy, M31, have proceeded alongside studies of Milky Way (MW) satellite galaxies over the past two decades. The story of M31 satellite discovery is familiar: just as advances in photometric surveys have unearthed many more MW satellites (e.g., V. Belokurov et al. 2007; A. Drlica-Wagner et al. 2015; B. P. M. Laevens et al. 2015; K. Bechtol et al. 2015; D. Homma et al. 2019), deep and comprehensive photometric surveys have similarly built an abundant census of faint satellites around M31 (e.g., A. W. McConnachie & M. J. Irwin 2006b; A. W. McConnachie et al. 2008; N. F. Martin et al. 2013; A. Doliva-Dolinsky et al. 2022).

Emerging studies of these satellites indicate that their properties are not entirely similar to those of MW dwarf galaxies (A. W. McConnachie & M. J. Irwin 2006a; C. M. Brasseur et al. 2011; M. L. M. Collins et al. 2014; A. Doliva-Dolinsky et al. 2023; A. Savino et al. 2023). Most notably in the ultrafaint regime ($< 10^5 L_\odot$), their star formation histories (SFHs) tend to be more extended than MW ultrafaint dwarf galaxies (UFDs), suggesting that the low-mass galaxies are not uniformly affected by reionization (e.g., D. R. Weisz et al. 2014b; M. Monelli et al. 2016; A. Savino et al. 2023). The distinct SFHs of M31 satellites suggest that they experienced different chemical enrichment histories than MW UFDs. The evidence of this difference should be reflected in their stellar abundance patterns (e.g., distributions in [Fe/H], [α/Fe]), which encode information on the baryonic processes (e.g., the balance of inflows vs. outflows) that shaped a galaxy's evolution (e.g., B. H. Andrews et al. 2017; D. H. Weinberg et al. 2017; N. R. Sandford et al. 2024). Unfortunately, the large distance of the M31 satellites means that only the

brightest have ample robust stellar abundances measured from spectroscopy (N. Ho et al. 2012; L. C. Vargas et al. 2014; K. Kvasova et al. 2024). In fainter M31 satellites, only a handful of individual stars are bright enough for ground-based measurements (E. N. Kirby et al. 2020).

Photometric metallicity measurement techniques enable recovery of stellar metallicities for fainter stars lower down a galaxy's luminosity function by imaging in filters specifically designed to trace strong, metallicity-sensitive features in stellar spectra. They are an important complement to ongoing spectroscopic efforts to study the M31 dwarf population in great detail. This is a well-established technique that has been utilized for decades of MW studies, including to the present (e.g., B. Strömgren 1966; T. C. Beers et al. 1985; E. Starkenburg et al. 2017; A. Chiti et al. 2021a; N. F. Martin et al. 2023). From space, our team has already applied this imaging technique using Hubble Space Telescope (HST)/WFC3 imaging in the narrowband F395N filter, targeting the Ca H and K lines, to great success for MW UFDs (S. W. Fu et al. 2022, 2023) and to a distant isolated dwarf galaxy on the outskirts of the Local Group (LG; Tucana; S. W. Fu et al. 2024). The singular and singularly important contribution HST has made to the field of resolved stellar metallicity measurements is enabling measurements for stars 1–2 mag fainter than currently reachable by any ground-based spectroscopic or imaging facility to date.

In this paper, we present results from an HST program to apply the narrowband Ca H and K photometric imaging technique to two of M31's UFD satellite galaxies: Andromeda XVI (And XVI) and Andromeda XXVIII (And XXVIII).

And XVI is a rare system among the ∼100 cataloged low-mass galaxies in the LG (R. Ibata et al. 2007). Its stellar mass ($M_V = -7.5$, $M_\star \sim 10^5\ M_\odot$) places it among the brightest "ultrafaint" dwarf galaxies (UFDs) known in the LG (J. D. Simon 2019). At 280 kpc from M31 (A. Savino et al. 2022), And XVI lies beyond the spiral's virial radius. While the vast majority of UFDs are characterized by metal-poor (MP), ancient stellar populations that are associated with formation at times during or prior to reionization, deep HST imaging revealed that And XVI only had a low level of star formation at the earliest times and instead experienced extended star formation that lasted until ∼6 Gyr ago ($z \lesssim 1$; D. R. Weisz et al. 2014b; M. Monelli et al. 2016; E. D. Skillman et al. 2017). And XVI's prolonged SFH provided a new link between the faintest UFDs that appear to be quenched by reionization and more massive "classical" dwarfs whose growth appears unaffected by reionization. Detailed stellar metallicity distribution functions (MDFs) are a crucial component of characterizing the physics driving these remarkable properties, but prior to this work there have been no resolved stellar metallicity measurements in And XVI: Keck/DEIMOS spectroscopy was only able to obtain mean metallicity measurements $\langle[\text{Fe/H}]\rangle = -2.1 \pm 0.2, -1.9 \pm 0.2$, and -2.0 ± 0.1 by stacking low signal-to-noise ratio (S/N) stellar spectra (B. Letarte et al. 2009; M. L. M. Collins et al. 2013, 2015).

And XXVIII ($M_\star \sim 10^{5.5}\ M_\odot$) is a faint galaxy located ∼370 kpc from the center of M31 (C. T. Slater et al. 2011; A. Savino et al. 2022). More massive than And XVI, its SFH is also more strongly weighted to old ages: the majority of its stars formed 12 Gyr ago, with a small remaining fraction forming as recently as 8 Gyr ago; these SFH properties are comparable to those of the Ursa Minor and Draco dSphs (E. D. Skillman et al. 2017). Using Keck/DEIMOS

spectroscopy, C. T. Slater et al. (2015) measured calcium triplet (CaT) metallicities for 13 stars in And XXVIII, finding $\langle[\text{Fe/H}]\rangle = -1.84 \pm 0.15$ dex and $\sigma_{[\text{Fe/H}]} = 0.65 \pm 0.15$ dex. While these measurements are illustrative for tracing out broad properties of its MDF, they are not well sampled enough to fully trace out its shape and define the tails.

Studying just these two galaxies can offer insight on star-forming physics in dwarf galaxies of different mass and over different timescales in an environment that is not the MW halo. Robust stellar metallicities are a critical missing piece to this emerging picture. The properties of And XXVIII and And XVI formed the basis for an approved pilot HST program leveraging Ca H and K imaging on WFC3/UVIS to measure their stellar MDFs. In this paper, we present the first extensive set of resolved stellar metallicities in And XVI and And XXVIII. We present our observations in Section 2, our metallicity inference method in Section 3, and our results in Section 4. We discuss the implications of our results in Section 5 and conclude with forward-facing remarks in Section 6.

2. Observations and Data Reduction

We acquired new F395N imaging using HST WFC3/UVIS for And XVI and And XXVIII as part of HST-GO-16686 (PI: Weisz). Our aim was to measure metallicities for ∼100 red giant stars in each system. Accordingly, the nominal target depth of this program aimed to collect sufficiently high S/N ($\gtrsim$10) F395N imaging to approximately the depth of the HB ($M_{\text{F475W}} \sim +0.5$). This depth goal is slightly brighter in the more luminous systems, as reaching the horizontal branch (HB) was not necessary to acquire at least 100 stars.

Imaging was acquired between 2022 November 21 and 2023 January 15. We summarize our observations in Table 1. We also targeted And XV, but the observations, as well as the repeat observations, failed owing to issues with guide star acquisition.

We centered our UVIS fields on existing HST/Advanced Camera for Surveys (ACS) broadband F475W and F814W imaging from the ISLAnds program (E. D. Skillman et al. 2017). We used subpixel dithers to sample the point-spread function (PSF), improve cosmic-ray rejection, etc., and used the post-flash level (FLASH = 20) advised by STScI to mitigate charge transfer efficiency effects. We observed And XI for 11 orbits and And XXVIII for nine orbits. Visits for both sets of observations consisted of one to two orbits. Long integrations were used in order to increase the S/N for bright stars in order to aid with astrometric alignment of the images. More observational details can be found in our public Phase II file. Figure 1 shows the WFC3 footprint overlaid on the ACS image of each galaxy, overplotted with elliptical contours at 1, 2, and 3 half-light radii.

We performed PSF photometry simultaneously on all F395N, F475W, and F814W HST images of And XVI and And XXVIII using DOLPHOT (A. E. Dolphin 2000; A. Dolphin 2016). DOLPHOT is a crowded field stellar photometry package that is widely used to analyze resolved star observations of nearby galaxies and star clusters. We followed the DOLPHOT reduction procedure that our team has applied to HST Ca H and K studies of other nearby galaxies (S. W. Fu et al. 2022, 2023, 2024).

Following S. W. Fu et al. (2023), we culled the raw DOLPHOT output in order to select high-quality stars. We created a noise model for our data using ∼500,000 artificial star

Table 1
Dwarf Galaxy Characteristics

Parameter	And XVI	And XVI Reference	And XXVIII	And XXVIII Reference
R.A. (deg.)	14.8762500	N. F. Martin et al. (2016)	338.1716667	C. T. Slater et al. (2011)
decl. (deg.)	32.3761111	”	31.2161667	”
Ellipticity	0.29 ± 0.08	”	0.34 ± 0.13	”
P.A. (deg.)	99 ± 9	”	39 ± 16	”
r_h (arcmin)	1.0 ± 0.1	”	1.11 ± 0.21	”
$E(B-V)$	0.0568	E. F. Schlafly & D. P. Finkbeiner (2011)	0.0758	E. F. Schlafly & D. P. Finkbeiner (2011)
$(m-M)_0$ (mag)	23.57 ± 0.08	A. Savino et al. (2022)	24.36 ± 0.05	A. Savino et al. (2022)
M_V (mag)	-7.5 ± 0.03	”	$-8.8\,^{+0.4}_{-1.0}$	”
Luminosity ($\log_{10}L_\odot$)	4.9	”	5.5	”
$M_\star$ ($\log_{10}M_\odot$)	5.2	”	5.8	”
$D_\odot$ (kpc)	517 ± 19	”	745 ± 17	”
D_{M31} (kpc)	280^{+26}_{-27}	”	$368.8^{+7.8}_{-7.3}$	”
r_h in WFC3 FOV	2.7	This work	2.43	This work
F475W exp. time (s)	17194	E. D. Skillman et al. (2017)	26360	E. D. Skillman et al. (2017)
F814W exp. time (s)	13622	”	20880	”
F395N exp. time (s)	30154	This work	24869	This work
F395N obs. dates	Jan. 9-15, 2023	”	Nov. 21-23, 2022	”

Note. Observational characteristics of And XVI and And XXVIII. F395N data are taken for this work from HST GO-16686 (PI: Weisz). Archival broadband data are from the ISLAndS program (E. D. Skillman et al. 2017): GO-13028 (PI: Skillman) for And XVI (D. R. Weisz et al. 2014a; M. Monelli et al. 2016; E. D. Skillman et al. 2017), and GO-13739 (PI: Skillman) for And XXVIII.

tests (ASTs). The ASTs were distributed across the red giant branch (RGB) in F395N, F475W, and F814W, following the method described in S. W. Fu et al. (2024).

The left column of Figure 2 shows the broadband F475W − F814W color−magnitude diagrams (CMDs) of And XVI (top) and And XXVIII (bottom), zoomed in on their RGBs. We use the kinematic catalogs of each dwarf used in M. L. M. Collins et al. (2013, 2014, 2015) to remove two radial velocity interlopers in And XXVIII and four interlopers in And XVI for stars as faint as F475W ∼ 24; these stars are represented in the figure as cyan circles. We color-code the RGB stars used in this analysis by their F395N S/N. The F395N data reached the anticipated depth (i.e., approximately the HB) in both cases. Following S. W. Fu et al. (2023), we only measure metallicities for stars with $S/N_{F395N} \geqslant 10$. After measuring metallicities, we remove additional obvious interlopers by hand, namely, stars whose metallicities are inconsistent with their color on the CMD (e.g., metal-rich (MR) stars on the blue end of the RGB). This resulted in the removal of an additional three stars in And XXVIII and four stars in And XVI. These vetting results are within the range of predicted MW foreground contamination from the TRILEGAL model (E. Vanhollebeke et al. 2009), which we expect to have a minimal contribution to the MDFs owing to the small field of view (FOV) of HST (S. W. Fu et al. 2023).

In total, our sample includes 191 stars in And XXVIII and 95 stars in And XVI.

3. Metallicity Property Determination

3.1. Individual Stellar Metallicities

We measure stellar metallicities following the procedures laid out in S. W. Fu et al. (2023), with adaptations adopted in S. W. Fu et al. (2024) for the case of dwarf galaxies with extended SFHs. Here we briefly summarize this technique.

We construct a set of basis functions from the MESA Stellar Isochrones and Tracks (MIST) stellar evolution models

(A. Dotter 2016; J. Choi et al. 2016) over a range of metallicities ($-4 \leqslant [\text{Fe/H}] \leqslant 0$) for a 13 Gyr stellar population. These models are the forthcoming v2 models that are scaled to the N. Grevesse & A. J. Sauval (1998) solar abundances and include variations in [α/Fe]. Because the RGB is only weakly sensitive to age, the exact age adopted does not affect Ca H and K metallicity measurements. The basis functions are projected into the standard Ca H and K color–color space, as shown in the middle panels of Figure 2. The color space is pixelated (i.e., similar to a Hess diagram used in fitting CMDs). We adopt bins that are 0.025 in size in both color indices. Each basis function is then convolved with the noise model determined from the ASTs. We compare the location of each observed star in Ca H and K color–color space to each basis function, using a Poisson likelihood function and flat priors in [Fe/H].

We follow S. W. Fu et al. (2024) to account for the effects of varying α-elements. Specifically, for [Fe/H] < −2.0 we only use basis functions with [α/Fe] = +0.4, and for [Fe/H] > −1.0 we only use basis functions with [α/Fe] = +0.0. Finally, for the range $-2.0 \leqslant [\text{Fe/H}] \leqslant -1.0$ we use basis functions with [α/Fe] = +0.2. This criterion approximates the plateau, knee, and knee-to-ankle transitions known to exist in the [α/Fe] versus [Fe/H] diagrams of MW satellites (e.g., E. Tolstoy et al. 2009). As demonstrated in S. W. Fu et al. (2022), the choice of [α/Fe] introduces a shift in metallicity measurements. For example, adopting [α/Fe] = +0.4 instead of [α/Fe] = +0.0 causes the measured metallicity to be ∼0.2 dex more MR. In the current analysis technique, we do not consider any scatter in [α/Fe] at fixed [Fe/H]. In addition to random uncertainties on each star, we adopt a 0.2 dex systematic uncertainty owing to uncertainties in [α/Fe] and the impact of additional elements (e.g., S. W. Fu et al. 2023).

We evaluate the posterior distribution for each star using emcee (D. Foreman-Mackey et al. 2013). We use 50 walkers with a burn-in time of 50 steps per star and then sample 10^4 steps to fill out the posterior space. We assess convergence
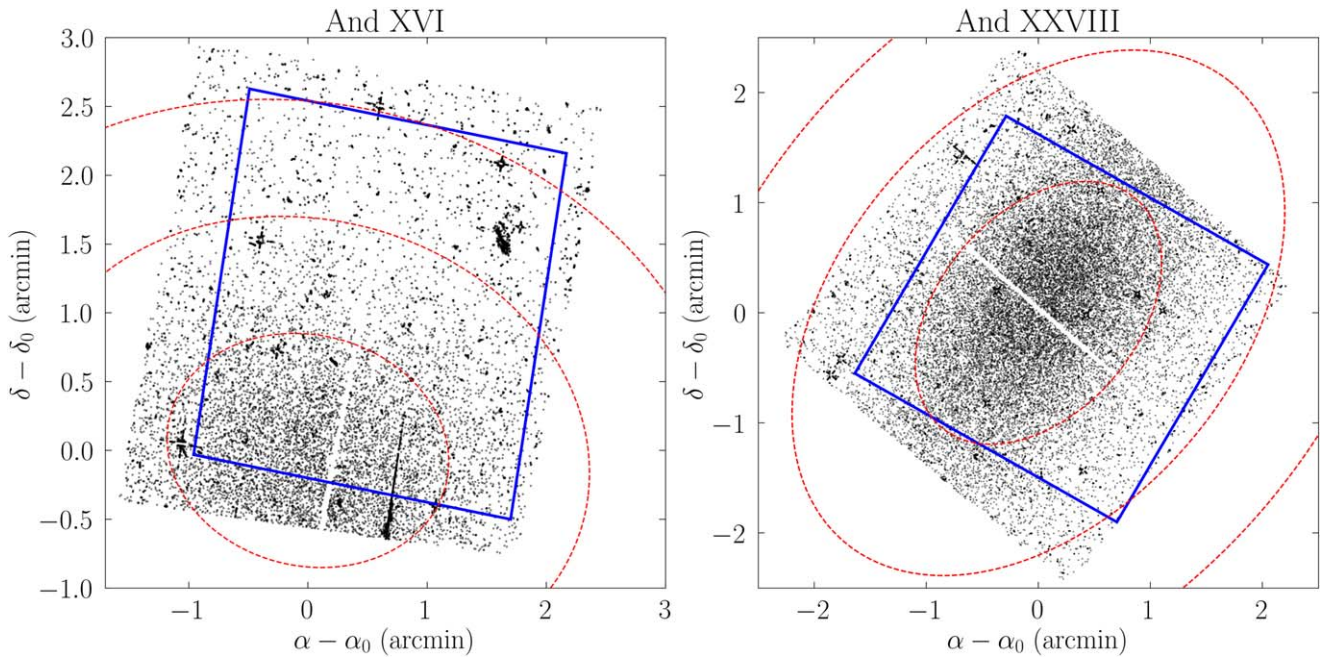
Figure 1. Illustrating the coverage of our HST imaging. The black dots are detected sources from the archival ACS archival image for each galaxy from which we measure broadband F475W and F814W photometry. The blue squares are the WFC3/F395N FOV. Each galaxy's elliptical half-light contours are plotted in red, corresponding to 1, 2, and 3 half-light elliptical radii.

using the Gelman−Rubin statistic (A. Gelman & D. B. Rubin 1992).

Following past work, for stars with probability distribution functions (pdf's) that have clear peaks and are within the metallicity grid, we report the median of each pdf as the metallicity of the star and the 68% confidence interval for the statistical uncertainty. The statistical uncertainty is set by spacing in the MIST Ca H and K color tracks and photometric uncertainty. We sum the statistical uncertainties in quadrature with an additional 0.2 dex systematic uncertainty in RGB star metallicities, as determined by S. W. Fu et al. (2023). The handful of extremely MP (EMP) stars in our sample (e.g., $[Fe/H] \leqslant -3.0$) that have either well- or poorly constrained pdf's (i.e., severe truncation at the grid boundary) tend to have larger statistical uncertainties owing to the closer spacing (i.e., decreased sensitivity) of Ca H and K tracks at lower metallicity. However, a star with very high photometric S/N can have a well-constrained metallicity below $[Fe/H] \leqslant -3.0$. For these stars, we increase the value of the systematic uncertainty to 0.5 dex to reflect challenges in accurately modeling MP stars.

3.2. MDF Summary Statistics

We compute summary statistics (e.g., fit a Gaussian profile) for the MDFs of And XVI and And XXVIII and spatial subpopulations, following the methods described in S. W. Fu et al. (2024) and references therein. We compute the mean metallicity ($\langle[Fe/H]\rangle$) and metallicity dispersion ($\sigma_{[Fe/H]}$) of the MDF by using a two-parameter Gaussian likelihood function. We assume a uniform prior on mean metallicity bounded by the most MP and MR star in the MDF. We also require the metallicity dispersion to be greater than zero. Similar to previous procedures, we adopt symmetric Gaussian uncertainties on individual measurements. We sample the posterior distribution using emcee (D. Foreman-Mackey et al. 2013), initializing 50 walkers to run for 10,000 steps. The

autocorrelation time is 50 steps, and we assess convergence using the Gelman-Rubin (GR) statistic.

For higher-order statistics such as skew and kurtosis, we also assume symmetric Gaussian uncertainties on individual metallicity measurements and use them to construct 10,000 realizations of the MDF. We measure the skew and kurtosis from each realization. We report final skew and kurtosis measurements as the median of the overall distribution, with lower and upper uncertainties set by the 16th and 84th percentiles, respectively. We present our table of summary statistics in Table 2 and our table of individual stellar metallicities in Table 3.

3.3. Measuring Metallicity Gradients

The spatial extent of our imaging enables us to characterize spatial metallicity trends across each galaxy. Thus, we also quantify the strength of the gradient as the slope ($\nabla_{[Fe/H]}$) obtained by fitting a line to individual stellar metallicities as a function of elliptical R_e from the center. Specifically, we follow the procedure outlined in D. W. Hogg et al. (2010) and implemented in S. W. Fu et al. (2024), which assumes Gaussian uncertainties on our measurements. We also fit the intercept of the line ($[Fe/H]_0$) and marginalize over an additional parameter f that is the fractional underestimation of measurement uncertainties. We assume uniform priors over the slope, intercept, and logarithmic fractional uncertainty. We sample the distribution using emcee by running 32 walkers for 10,000 steps. The burn-in time is about 50 steps. We assess convergence using the GR statistic.

4. Results

We present the results of our MDF measurements. The middle column of Figure 2 presents our sample in the color–color space defined by broadband color F475W − F814W and the *Pristine*-like color index (E. Starkenburg et al. 2017;
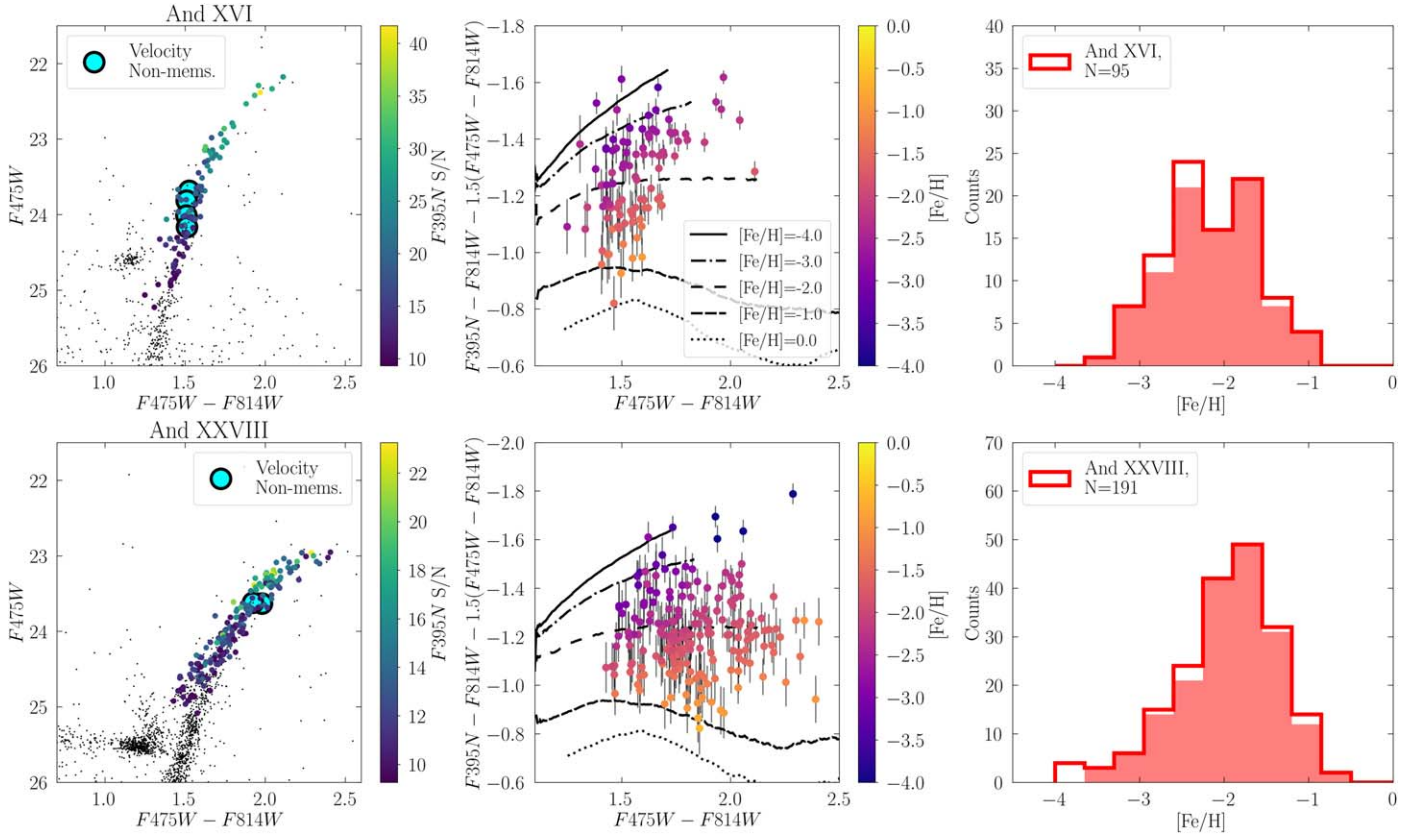
Figure 2. Presenting the CMD, Ca H and K color data, and resulting MDF for And XVI (top row) and And XXVIII (bottom row). Left column: broadband CMD of each galaxy, centered on its RGB, with stars analyzed color-coded by their F935N S/N. Stars in cyan circles are velocity interlopers determined using the data sets of M. L. M. Collins et al. (2013, 2014, 2015). Middle column: the position of analyzed stars in the *Pristine*-like color–color space, color-coded by their inferred metallicities. Monometallic Ca H and K tracks, convolved by the AST error profile of a star of median luminosity in each galaxy's sample, are overplotted to guide the eye. Since stars of different luminosity have different AST error profiles, the Ca H and K model tracks used to infer the metallicity of each star may be different from the ones presented here. Some of these metallicities are inferred upper limits due to either falling at the edge of the model grid for bright stars or being low S/N for fainter stars. Right column: the resulting MDF for each galaxy. Filled histograms are well-constrained measurements, and open histograms are stars for which we can only derive an upper limit.

F395N − F475W − 1.5(F475W − F814W)). Table 2 summarizes our global metallicity measurements. We present individual metallicities in Table 3 and candidate EMP stars in Table 4. In the subsequent subsections, we discuss results for individual galaxies.

4.1. And XVI

The top row of Figure 2 shows the broadband CMD of our member stars (left), their position on the Ca H and K color space with a representative set of AST-convolved Ca H and K monometallic tracks (middle), and the resulting MDF constructed from measurements of 95 stars (right). The stars in our MDF span a range from −3.5 to −1, with the majority of them between −2.5 and −1.5 (57 stars, 60%). Eleven (12%) stars have metallicities above −1.5. Seven stars (7%) have metallicities below −3; we designate these stars as EMP candidates. We measure an overall mean metallicity of $\langle[\mathrm{Fe/H}]\rangle = -2.17^{+0.05}_{-0.05}$ and quantify higher-order moments in the MDF. We measure a metallicity dispersion of $\sigma_{[\mathrm{Fe/H}]} = 0.33^{+0.07}_{-0.07}$. We also quantify the skew and kurtosis, but we do not find deviations from Gaussianity at a 2σ significance. Visually, there appears to be a double peak in its MDF (e.g., Figure 2) at ∼−2.5 and ∼−1.7, though the peaks may become washed out by moving a handful of stars within uncertainty into an adjacent bin.

To date, mean metallicity determinations of And XVI are from coaddition of S/N $\gtrsim 3$ spectra in the Ca II triple-line regime (B. Letarte et al. 2009; M. L. M. Collins et al. 2015, using the E. Starkenburg et al. 2010 calibration), which finds a mean metallicity of $\langle[\mathrm{Fe/H}]\rangle = -2.0 \pm 0.1$. Our mean metallicity is in good agreement with this coarser determination and places And XVI within 1σ scatter of the dwarf galaxy mass–metallicity relation (E. N. Kirby et al. 2013).

We measure the metallicity gradient in And XVI to $2R_e$. In the top row of Figure 3, we show the on-sky spatial distribution of stars, color-coded by our measured metallicity, and their distribution as a function of R_e. We measure a gradient of $\nabla_{[\mathrm{Fe/H}]} = -0.23 \pm 0.15$ dex R_e^{-1}. We consider the implications of this measurement as tentative evidence for a metallicity gradient and discuss its implications further in Section 5.

4.2. And XXVIII

We present our sample and the resulting inferred MDF in the bottom row of Figure 2. The stellar metallicities span a range from as low as −4 to as MR as −0.5. We identify 12 (6%) stars below −3 that we flag as EMP candidates for spectroscopic follow-up. Eight stars (4%) are more MR than −1.0. The MDF is peaked at ∼−1.8, and a majority of the stars (101; 53%) are between −2.0 and −1.0. We measured a mean metallicity of $\langle[\mathrm{Fe/H}]\rangle = -1.95^{+0.04}_{-0.04}$ and dispersion $\sigma_{[\mathrm{Fe/H}]} = 0.34^{+0.05}_{-0.05}$. We

Table 2
Metallicity Properties of And XVI and And XXVIII

Feature	Parameter	And XVI	And XXVIII
Global MDF	N	95	191
	$\langle[Fe/H]\rangle$	$-2.17^{+0.05}_{-0.05}$	$-1.95^{+0.04}_{-0.04}$
	$\sigma_{[Fe/H]}$	$0.33^{+0.07}_{-0.07}$	$0.34^{+0.05}_{-0.05}$
	Skew	$-0.14^{+0.25}_{-0.24}$	$-0.59^{+0.17}_{-0.18}$
	Kurtosis	$0.21^{+0.53}_{-0.38}$	$-0.76^{+0.49}_{-0.39}$
Metallicity gradient	R_e extent	2	2
	$\nabla_{[Fe/H]}$ (dex R_e^{-1})	-0.23 ± 0.15	-0.46 ± 0.10
	$\nabla_{[Fe/H]}$ (dex arcmin^{-1})	-0.27 ± 0.14	-0.30 ± 0.10
	$\nabla_{[Fe/H]}$ (dex kpc^{-1})	-1.8 ± 0.9	-1.39 ± 0.44
Inner Re	N	72	144
	$\langle[Fe/H]\rangle$	$-2.15^{+0.07}_{-0.07}$	$-1.86^{+0.04}_{-0.04}$
	$\sigma_{[Fe/H]}$	$0.37^{+0.08}_{-0.08}$	$0.33^{+0.06}_{-0.07}$
	Skew	$-0.17^{+0.27}_{-0.26}$	$-0.52^{+0.23}_{-0.24}$
	Kurtosis	$0.15^{+0.55}_{-0.40}$	$1.02^{+0.73}_{-0.54}$
Outer Re	N	23	47
	$\langle[Fe/H]\rangle$	$-2.23^{+0.10}_{-0.10}$	$-2.28^{+0.10}_{-0.11}$
	$\sigma_{[Fe/H]}$	$0.25^{+0.14}_{-0.14}$	$0.52^{+0.11}_{-0.10}$
	Skew	$-0.09^{+0.48}_{-0.49}$	$-0.39^{+0.27}_{-0.26}$
	Kurtosis	$-0.13^{+0.96}_{-0.6}$	$-0.15^{+0.55}_{-0.40}$

Note. Summarizing metallicity properties of And XVI and And XXVIII derived from this work, along with the number of stars used to infer each property.

also find that the MDF of And XXVIII is skew-negative above 3σ significance—this is reflected in the MDF, which shows a long MP tail.

Our results expand significantly on C. T. Slater et al. (2015), who measured individual metallicities for 13 And XXVIII stars using Gemini/GMOS spectroscopy. They measure stellar metallicities using the R. Carrera et al. (2013) CaT calibration and Gaussian equivalent widths of the strongest two CaT lines. Their stars span a range similar to ours: -3.0 to -0.5. Due to their sparse number sampling, the stars are evenly distributed across this range. From this data set, they measured $\langle[Fe/H]\rangle = -1.84 \pm 0.15$, which is in good agreement with our mean metallicity measurement. Their metallicity dispersion measurement of 0.65 ± 0.15 disagrees with our measurement by 2σ. This discrepancy is in part due to the improved sampling of our MDF about the mean. Spatial sampling also matters here, given the strong metallicity gradient in And XXVIII: the broader spatial coverage of the C. T. Slater et al. (2015) data set gives MP stars more weight in the MDF, therefore broadening the dispersion.

Of the seven stars that we have in common with C. T. Slater et al. (2015), our metallicities appear to be more MR by ~ 1 dex, but this disagreement is also within their uncertainties (~ 0.5–1.0 dex). The formal level of agreement between our measurements is 1σ. As shown in Figure 6 of S. W. Fu et al. (2024), our Ca H and K metallicities are generally in agreement with CaT metallicities from the literature, which themselves are derived from different implementations of the CaT calibration.

We resolve a strong gradient for And XXVIII of $\nabla_{[Fe/H]} = -0.46 \pm 0.10$ dex R_e^{-1}. We present the spatial distribution of stars and their metallicity as a function of R_e in Figure 3. Here the spatial concentration of MR stars in

comparison to MP stars is apparent even by eye. We attempted to formally measure the scale radii of the MP and MR stars, but we did not find a difference—this is likely because our data do not span sufficient area across the galaxy. Our measurement shows that there is a ~ 0.9 dex difference in mean metallicity between the population at the center of the galaxy and the population out at $2R_e$, across ~ 430 pc. We explore the implications of this gradient more in Section 5.

5. Discussion

5.1. MDFs: Context and Interpretation

Within the M31 satellite system, the most well-sampled stellar spectroscopic measurements have mostly been made in the more massive satellites (L. C. Vargas et al. 2014; N. Ho et al. 2015; K. Kvasova et al. 2024). Due to the difficulty of measuring metallicities for individual stars at the large distance of M31 satellites, most metallicities to date are measured by stacking low-S/N stellar spectra or using estimates from broadband photometry (e.g., N. F. Martin et al. 2014; M. L. M. Collins et al. 2015). These studies report mean metallicities from the result of spectral stacking and provide little information on MDFs.

Of the few faint M31 dwarfs with individual star spectroscopic metallicities (E. N. Kirby et al. 2020), in terms of stellar mass, And V ($M_\star = 10^{5.8} M_\odot$, 81 stars out to $2.5R_e$) is closest to And XXVIII and And X ($M_\star = 10^{5.1} M_\odot$, 21 stars out to $1.5R_e$) is closest to And XVI. The mean metallicities of the dwarf galaxies in each respective comparison pair are comparable, placing them within scatter on the universal dwarf galaxy mass–metallicity relation. Like And XXVIII, And V also has an MDF with a long MP tail. The MDF of And X is also symmetric like that of And XVI but does not include any stars more MR than -1.5. The MDFs of And V and And X both have three stars below $[Fe/H] < -3.0$. The percentages of EMP stars in And V and And XXVIII are similar. And X has a higher fraction of EMP stars than And XVI, although the sample size of And X's MDF is smaller. Due to their large distances and weak lines, EMP stars in the M31 satellite system have not been extensively identified in detail in the way that they have been in, e.g., MW satellites (E. Starkenburg et al. 2013). The EMP candidates we designate in this study will be valuable spectroscopic follow-up targets in the era of ELT spectroscopy.

5.1.1. And XXVIII

From the compilation of properties of MW satellites by E. N. Kirby et al. (2013), the closest luminosity analogs to And XXVIII ($L \sim 10^{5.5} L_\odot$) are Ursa Minor ($\langle[Fe/H]\rangle = -2.13$, $\sigma_{[Fe/H]} = 0.43$), Draco ($\langle[Fe/H]\rangle = -1.98$, $\sigma_{[Fe/H]} = 0.42$), and Canes Venatici I ($\langle[Fe/H]\rangle = -1.91$, $\sigma_{[Fe/H]} = 0.44$). Comparing qualitatively to these MDFs, the MDF of And XXVIII resembles those of Draco and Canes Venatici I in that the MDFs of all three galaxies are characterized by long, MP tails. In contrast, the MDF of Ursa Minor is more symmetric, with a slightly longer MR tail. Quantitatively, the mean metallicity of And XXVIII is comparable to those of all three galaxies, although its metallicity dispersion is smaller by ~ 0.1 dex. This smaller dispersion is due to the MP side of the MDF: we assume large uncertainties on our EMP star candidates, which downweighs the most MP stars' contributions to the metallicity dispersion. A reinference of And XXVIII's MDF without

assuming our adopted systematic uncertainties, which mostly affect the most MP stars, yields $\langle[\mathrm{Fe/H}]\rangle = -1.99 \pm 0.05$ and $\sigma_{[\mathrm{Fe/H}]} = 0.54 \pm 0.04$. This suggests that differences in σ for the MW satellites and And XXVIII are not significant. The higher-order moments in their MDFs are also comparable.

5.1.2. And XVI

At $L \sim 10^{4.9}\,L_\odot$, And XVI is classified as one of the most luminous UFDs ($L < 10^5\,L_\odot$; J. D. Simon 2019) in the LG . Its closest luminosity analog among MW UFDs is Eri II ($L \sim 10^{4.8}\,L_\odot$, $\langle[\mathrm{Fe/H}]\rangle = -2.63 \pm 0.06$, $\sigma_{[\mathrm{Fe/H}]} = 0.26^{+0.08}_{-0.09}$; D. Crnojević et al. 2016; T. S. Li et al. 2017; S. W. Fu et al. 2022). Compared to Eri II, the MDF of And XVI is more MR by 0.5 dex. Since MW UFDs fainter than Eri II also have mean metallicities of about $[\mathrm{Fe/H}] \sim -2.6$ (S. W. Fu et al. 2023), And XVI is more MR than MW UFDs by a similar amount. While And XVI also has an MP tail, it also has a higher fraction of stars more MR than $[\mathrm{Fe/H}] = -2.0$ and, subsequently, a higher $\sigma_{[\mathrm{Fe/H}]}$. This may be attributable to its extended SFH relative to Eri II, which allows more time for subsequent generations of stars to enrich. The gradual fall-off of And XVI's MDF suggests that it likely did not experience rapid truncation of SF (e.g., via ram pressure stripping or strong feedback) during the final epochs of its star formation.[15]

The HST CMD-based SFH of And XVI shows that it had two major episodes of SFH: one at 13 Gyr ago that formed $\sim 50\%$ of its stellar mass before being quenched at a time corresponding to reionization, and then another SF at 8 Gyr that built up the remainder of the galaxy's stellar population (D. R. Weisz et al. 2014b; M. Monelli et al. 2016; E. D. Skillman et al. 2017). Given this SFH, a speculative interpretation of its potentially double-peaked MDF is that the MP peak ($[\mathrm{Fe/H}] = -2.5$) and MR ($[\mathrm{Fe/H}] = -1.7$) peak respectively correspond to its first and second major episodes of star formation. Following this narrative thread, and assuming a present-day $M_\odot/L_\odot = 2$, And XVI at 13 Gyr ago may have had $M_\star \sim 8 \times 10^4\,M_\odot$, with a mean stellar metallicity of -2.5. At this time, its stellar mass and mean metallicity would have been very comparable to the present-day mass of MW UFDs CVn II, Hya II, and Eri II (E. Sacchi et al. 2021; D. R. Weisz et al. 2023; S. W. Fu et al. 2023).

However, the age–metallicity relation (AMR) of And XVI from the HST CMD modeling measured by M. Monelli et al. (2016) is flat and therefore does not suggest metallicity evolution as a function of time. The uncertainties on the metallicities from the AMR encompass the peaks of the MDF, so it is possible that SFH studies may not have the metallicity sensitivity to be able to resolve this enrichment scenario. Moreover, M. Monelli et al. (2016) only use solar-scaled stellar models, which may not be accurate for the lower-metallicity stars in And XVI, possibly affecting the metallicity inference. Obtaining more stellar metallicities through deeper HST Ca H and K imaging of the current And XVI field or HST Ca H and K and broadband imaging across a different field in the galaxy may be the best way to determine whether the double-peaked feature in the MDF is real.

5.2. Metallicity Gradients in M31 Dwarf Galaxies

From 95 stars spread over $2R_e$, we measure a metallicity gradient in And XVI at 1.5σ significance. The identification of a gradient in And XVI is interesting, as the extent to which lower-mass galaxies like UFDs can host metallicity gradients, and what the origins of their gradients could be, is still unknown. There are many ongoing efforts to detect stars in the outskirts of MW UFDs, which tend to be even lower in stellar mass than And XVI (F. Waller et al. 2023; N. Longeard et al. 2023; E. A. Tau et al. 2024; X. Ou et al. 2024). Among these studies, two have suggested the existence of metallicity gradients in the studied UFDs. In Eri II, the metallicities of 67 RR Lyrae stars out to $2R_e$ trace out a gradient of ~ 0.3 dex R_e^{-1} (C. E. Martínez-Vázquez et al. 2021).[16] In the lower-mass Tucana II ($L_\star \sim 3 \times 10^3\,L_\odot$), the metallicity difference between the inner regions ($[\mathrm{Fe/H}] = -2.6$) and the two MP ($[\mathrm{Fe/H}] = -3.0$) stars beyond $2.5R_e$ forms the basis for the gradient (A. Chiti et al. 2021b). The differential variations here are comparable to the gradient strength that we measure in And XVI.

Given the intrinsic difficulty of detecting metallicity gradients in faint galaxies (e.g., few stars available for targeting, coverage and selection effects), we consider the implications of a metallicity gradient in And XVI. One of its most notable differences from other known UFDs is an extended SFH: MW UFDs universally have old stellar populations of ~ 13 Gyr (D. R. Weisz et al. 2014a; T. M. Brown et al. 2014; E. Sacchi et al. 2021), as do the majority of M31 UFDs with published SFHs (A. Savino et al. 2023). Simulations have posited that metallicity gradients can form in dwarf galaxies more massive than And XVI via mechanisms that require an extended SFH, e.g., stellar feedback from young, short-lived stars that preferentially push old, MP stars to a galaxy's outskirts (FIRE simulations; K. El-Badry et al. 2016; F. J. Mercado et al. 2021), and gas accretion that triggers centrally concentrated star formation (e.g., J. Schroyen et al. 2013). The detection of a gradient in And XVI, which lies at the threshold of the nominal division ($M_\star \sim 10^5\,M_\odot$) between UFDs and classical dwarf galaxies, may suggest that similar physics can be significant in shaping the evolution of UFDs at the mass of And XVI. As we discuss later in this section, additional theoretical work is necessary to determine the mechanisms for stellar metallicity gradient formation in such low-mass systems.

We resolve a strong, highly significant (4.6σ) metallicity gradient in And XXVIII, where the average metallicity at the center of the galaxy is more MR than stars at $2R_e$ by 0.9 dex. A more general population gradient in And XXVIII was also observed by C. T. Slater et al. (2015) in the different spatial concentrations of its red and blue horizontal branch stars. In addition, stars between $1R_e$ and $2R_e$ in And XXVIII have a larger metallicity dispersion than stars in its center, which is also seen in the spatially extended MP population of Ursa Minor (A. B. Pace et al. 2020). Among LG dwarf galaxies with population gradients, spatially compact MR populations and comparatively spatially diffuse MP populations can also have different kinematics (e.g., G. Battaglia et al. 2006; M. G. Walker et al. 2009; N. Kacharov et al. 2017; A. B. Pace

---

[15] A stark contrast is the MDF of the more massive And XVIII, which sharply truncates at $[\mathrm{Fe/H}] = -1.0$; this cutoff has been attributed to a sudden stop to star formation (K. Kvasova et al. 2024).

[16] Our own analysis of Eri II's inner R_e using HST Ca H and K imaging did not uncover a gradient (S. W. Fu et al. 2022). The area is small, and we did not consider α-enhancements in that analysis, which may contribute to our result.
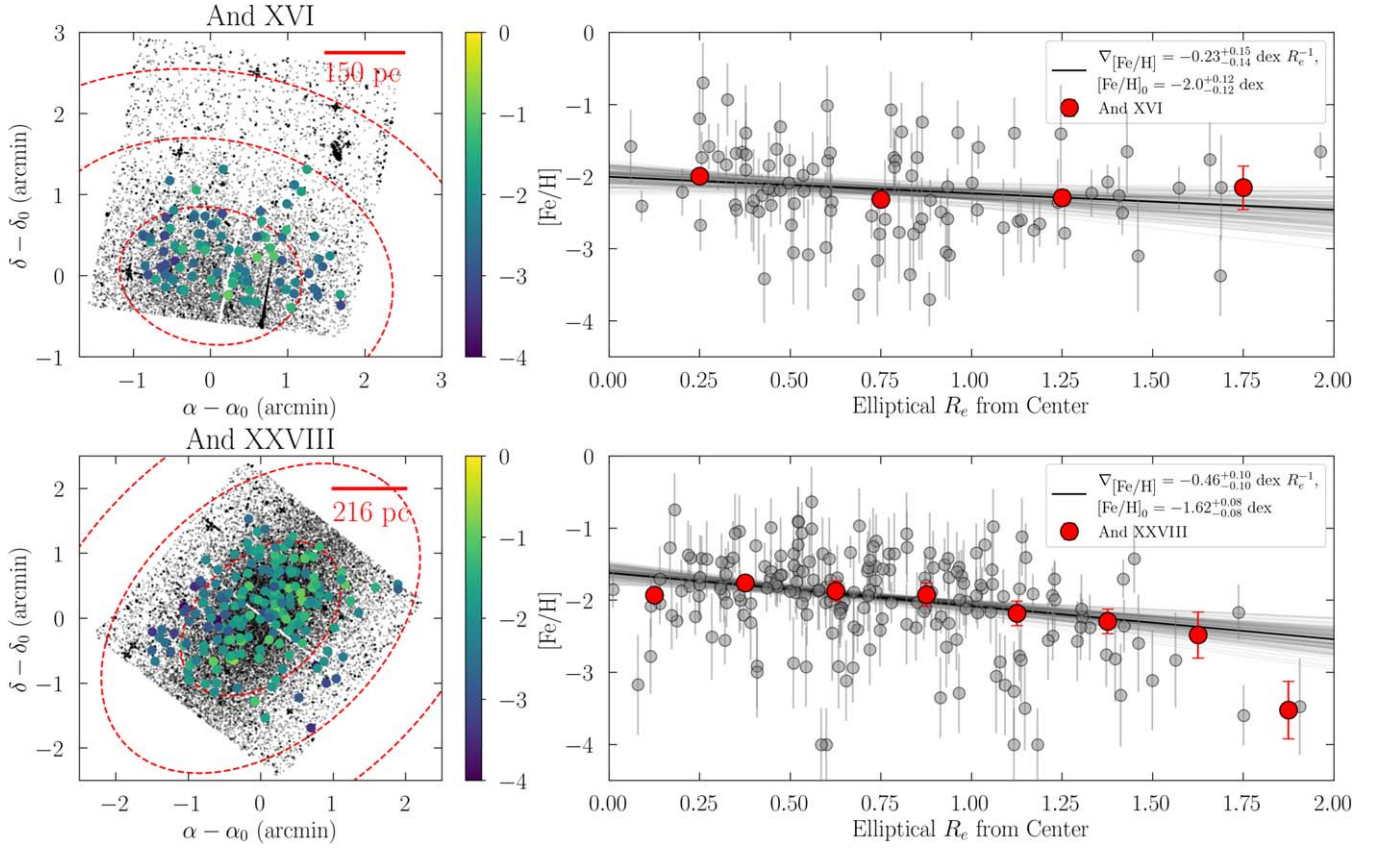
Figure 3. Left: spatial distribution of stars in And XVI (top) and And XXVIII (bottom), color-coded by their inferred metallicities. Also presented are each galaxy's half-light contours at $1R_e$, $2R_e$, and $3R_e$ and a scale bar indicating physical distance. Right: result of fitting a linear model to our data as a function of elliptical half-light radius. Gray circles are individual data points in each galaxy, while red circles are the mean metallicity in spatial bins of $0.5R_e$ for And XVI and $0.25R_e$ for And XXVIII. We are able to robustly recover a metallicity gradient for And XXVIII. We also tentatively detect a gradient in And XVI. These are among the few metallicity gradients of M31 satellites more generally and, for And XVI, one of the few gradients detected in UFDs to date.

et al. [2020]). The presence or absence of this feature may point to different origins for forming the gradient (e.g., kinematic differences suggestive to dwarf−dwarf mergers; S. Taibi et al. [2022]). In this context, And XXVIII is also an ideal target for spectroscopic studies to obtain kinematic information, enabling a full chemodynamic characterization of the system and its formation history.

Metallicity gradients are common among "classical" LG dwarf galaxies. They have been observed within galaxies spanning a range of kinematic properties, isolated/satellite status, and stellar mass (S. Taibi et al. [2022]). Within the M31 system, however, metallicity gradients have only been measured in three satellites to date: And II ($\nabla_{[Fe/H]}= -0.39 \pm 0.07$ dex R_e^{-1}) and NGC 185 ($\nabla_{[Fe/H]}= -0.20 \pm 0.03$ dex R_e^{-1}) from the L. C. Vargas et al. [2014] and N. Ho et al. [2015] data set that was reanalyzed by S. Taibi et al. [2022], and And XVIII ($\nabla_{[Fe/H]}= -0.23 \pm 0.03$ dex R_e; K. Kvasova et al. [2024]).[17]

---

[17] Despite measuring the gradient from only 38 stars, the reported uncertainties in And XVIII are smaller than from gradient measurements made with hundreds of stars as in the case of the previous work. K. Kvasova et al. [2024], as well as L. C. Vargas et al. [2014] and N. Ho et al. [2015], used a least-squares method to infer their gradients, which results in smaller gradient uncertainties due to assuming known Gaussian variance on individual stellar metallicities (D. W. Hogg et al. [2010]). For a more direct comparison with our inference approach, we instead adopt the S. Taibi et al. [2022] reanalysis where available, as we find from S. W. Fu et al. [2024] that their Gaussian process regression method produces comparable gradient measurements to ours.
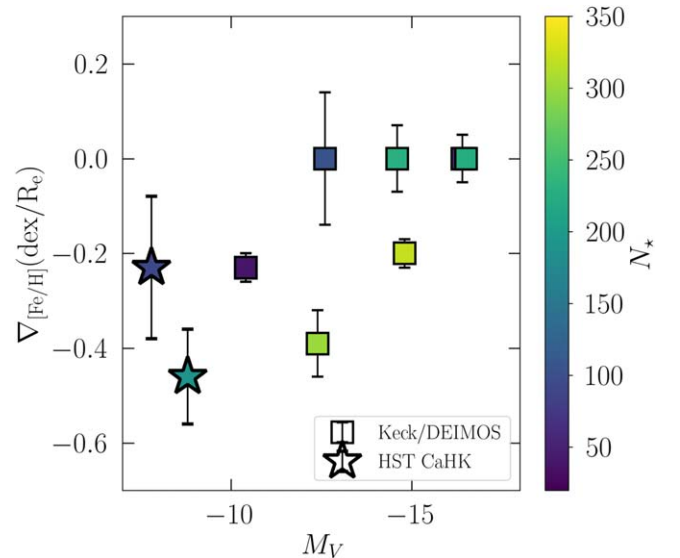

Figure 4. Contextualizing our gradient measurements for And XVI and And XXVIII in the current landscape of gradients in M31 dwarfs. Literature gradients for M31 satellites are from the reanalysis of the N. Ho et al. [2015] data set in S. Taibi et al. [2022]; NGC 205, NGC 185, NGC 147, And VII), and K. Kvasova et al. [2024]; And XVIII). The galaxies are color-coded by the number of stars used to make the gradient measurement. We have measured gradients in these faint galaxies using a comparable number of stars to what Keck/DEIMOS spectroscopy was able to reach in dwarf galaxies several orders of magnitude more luminous.
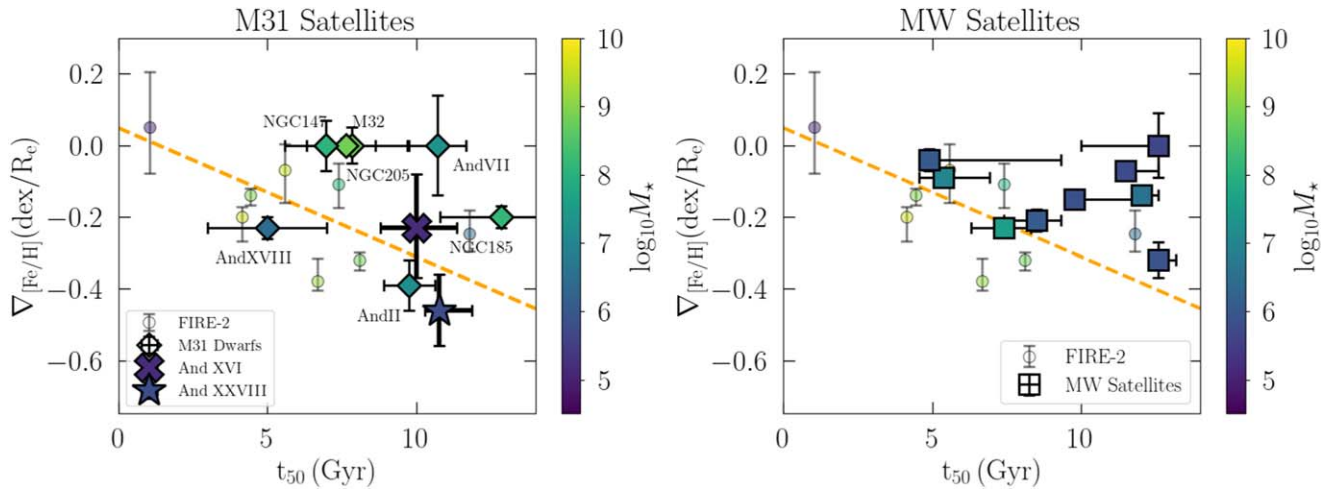
Figure 5. Comparing M31 and MW satellite metallicity gradients to predictions from the FIRE-2 simulations. Left: presenting gradients of M31 satellites relative to the age–metallicity gradient strength relation from FIRE-2 simulations (F. J. Mercado et al. 2021). All galaxies, simulated and observed, are color-coded by their stellar masses. The linear form of the relation is orange, and light-colored circles denote the publicly available FIRE-2 simulated galaxies. Diamonds are M31 satellites from the literature, and the cross and star are And XVI and And XXVIII, respectively. Our dwarf galaxy gradient measurements trace out the age–gradient relation. Right: presenting gradients of MW satellites as compared to the FIRE-2 simulations. The simulated relations are presented in the same fashion as in the previous panel. Gradient measurements are sourced from S. Taibi et al. (2022). The MW satellites show large scatter about the age–gradient relation.

In Figure 4, we emphasize the novelty of our measurements from this paper within the landscape of gradient measurements in M31 dwarfs. In more luminous M31 dwarf galaxies, Keck/DEIMOS spectroscopy has been used to constrain metallicity gradients from measurements of hundreds of stars. In fainter M31 satellites, there simply are not enough bright stars to construct comparably well populated MDFs using spectra. The Ca H and K based MDFs in this paper, however, can provide large samples of metallicities, enabling the construction of MDFs that are as robust as the more luminous M31 satellites.

Metallicity gradients are one of the few observationally accessible signatures of baryonic processes that shape both luminous and dark matter. For example, stellar feedback has long been invoked as a mechanism for transforming initially cuspy dark matter halos into cores (J. F. Navarro et al. 1996; F. Governato et al. 2010; S. Garrison-Kimmel et al. 2013; P. Madau et al. 2014). Through this mechanism, cored DM profiles would therefore be consistent with a ΛCDM universe, providing resolution to the long-standing "core–cusp" problem. As one example in the contemporary literature, the FIRE-2 simulations of isolated dwarf galaxies predict a relationship between gradient strength and mean stellar age in dwarf galaxies (F. J. Mercado et al. 2021) that would arise as a result of these feedback processes that also produce dark matter cores.

We show this relation in Figure 5 and compare it to data. In the left panel, we plot the linear form of the relation fit to F. J. Mercado et al. (2021) simulations, properties of the publicly available simulated FIRE dwarfs, and the gradient measurements of M31 dwarfs, including those derived in this work. With the exception of And XVIII (N. Kacharov et al. 2017), the mean galaxy ages (t_{50}) are taken from A. Savino et al. (2024, in preparation), who use deep CMDs from the HST survey of M31 satellites to measure SFHs and include reanalyses of CMDs from the literature (M. Geha et al. 2015; E. D. Skillman et al. 2017).

In the right panel, we compare the same relation against gradient measurements of MW satellites from the S. Taibi et al. (2022) analysis, with SFHs from D. R. Weisz et al. (2014a). All dwarfs, simulated and observed, are color-coded by their stellar

mass. One notable caveat to data interpretation here is that the area coverage of the SFH measurements and that of the spectroscopic gradient measurements are often different, with the gradient measurements spanning a larger area over the dwarf owing to the nature of spectroscopic targeting.

Our measurements of And XVI and And XXVIII appear to affirm the theoretical relation quite well. This is additionally noteworthy given that the relation was derived from simulations of isolated dwarfs, not satellites. This could be because the bulk of the metallicity information was in place at early times before many of these galaxies were bound satellites. The rest of the M31 satellites, as well as the MW satellites, appear to have large scatter about this relation. In particular, there are no galaxies with intermediate t_{50} that have strong gradients. The scatter in gradient strength is largest among galaxies with older stellar populations, ranging from nondetections to gradients as strong as -0.4 dex R_e^{-1}. One simple, qualitative interpretation of this picture is that old galaxies, with metallicity gradients in place in accordance with the age–gradient relation, had their gradients flattened through close passage(s) with a more massive host that preferentially removes their MP outskirts.[18] The extent to which And XVI and And XXVIII can be described by this scenario is unclear: both currently lie beyond the virial radius of M31, and their orbital histories about M31 are not constrained, due to the absence of proper motions. Detailed orbital histories of LG dwarf galaxies (E. Patel et al. 2020; A. B. Pace et al. 2022; G. Battaglia et al. 2022; P. Bennet et al. 2023) will be key to interpreting the various astrophysical origins of these observed gradients.

The theoretical age–gradient relation is compelling for its potential as an observational diagnostic of dark matter core formation in the dwarf galaxy population. However, its explanatory power needs refinement, given that environmental processes can also set metallicity gradients (A. Marcolini et al. 2008; L. V. Sales et al. 2010; A. Benítez-Llambay et al. 2016; L. Hausammann et al. 2019). Comparisons between

---

[18] Simulations of tidal stripping in dwarf galaxies show that the outskirts of the galaxy are removed first (e.g., J. Peñarrubia et al. 2008; R. Errani et al. 2022).

observation and theory also have additional caveats, in part due to ongoing challenges in simulating low-mass galaxies to high fidelity. The faintest publicly available FIRE-2 dwarf galaxy used to infer the age–gradient relation has $M_\star \sim 10^5\,M_\odot$ and t_{50} of 1 Gyr; these properties are not well matched to any LG dwarf galaxy regardless of environment, as galaxies in this mass range are dominated largely by old (<10 Gyr), or in some cases intermediate-age (~ 6 Gyr), stellar populations (e.g., D. R. Weisz et al. 2014a; C. Gallart et al. 2015; E. D. Skillman et al. 2017).

Notably, theoretical work, including the same simulations positing the age–gradient relation, have not identified galaxy stellar mass as a strong driving factor in gradient formation (J. Schroyen et al. 2013; Y. Revaz & P. Jablonka 2018; F. J. Mercado et al. 2021). This runs counterintuitive to observations, which show that more massive dwarf galaxies tend to have extended SFHs, younger stars, and lower t_{50} values (D. R. Weisz et al. 2014a). If stellar age indeed traces gradient strength, then this relation should also have an underlying stellar mass dependence. Given the near-uniformly old stellar ages of faint dwarf galaxies, particularly UFDs (D. R. Weisz et al. 2014a; T. M. Brown et al. 2014; C. Gallart et al. 2021; E. Sacchi et al. 2021; J. D. Simon et al. 2023), taking the age–gradient relation at face value would imply that nearly all galaxies with $M_\star < 10^5\,M_\odot$ should have strong metallicity gradients. The current empirical landscape of faint dwarf galaxy studies does not support this prediction, although obtaining high-fidelity gradient measurements for a large sample of UFDs has also been challenging.

Still, in the regime of classical dwarf galaxies, it is notable that the population-level behavior of metallicity gradients can be interpreted as the consequence of stellar-feedback-driven breathing modes that form dark matter cores (G. S. Stinson et al. 2007; K. El-Badry et al. 2016; F. J. Mercado et al. 2021). A natural question is how low in galaxy stellar or halo mass this framework can still apply and, relatedly, whether metallicity gradients in UFDs imply core formation at all. Indeed, whether UFDs host cores is still an open question: while simulations have suggested that stellar feedback is insufficient to sculpt cores in UFDs (e.g., F. Munshi et al. 2021; B. Azartash-Namin et al. 2024), observations of the Eri II UFD suggest strong feedback during star formation (C. Gallart et al. 2021; N. R. Sandford et al. 2024) and a marginally off-center star cluster that is expected to survive to $z = 0$ only if the galaxy has a cored DM profile (N. C. Amorisco 2017; J. D. Simon et al. 2021; D. R. Weisz et al. 2023).

The central mass profile of UFDs, as well as their reconciliability with small-scale predictions under CDM, remains an outstanding question (J. S. Bullock & M. Boylan-Kolchin 2017). On the observational side, gradient measurements in UFDs across a range of environments will be important for disentangling secular and external impacts on gradient formation. In particular, isolated low-mass galaxies ($M_\star < 10^6\,M_\odot$) with a range of SFHs such as Leo P, Tucana B, and Pavo—which are not expected to have interacted with a massive host throughout their lifetime—are important targets as a comparison foil for studies of MW and M31 satellites (K. B. W. McQuinn et al. 2015; D. J. Sand et al. 2022; M. G. Jones et al. 2023). By nature, these high-priority targets also tend to lie at the farthest distances, making spectroscopic studies to obtain adequately sampled stellar metallicity measurements, or stellar velocities for dynamical mass profile

studies, especially challenging. As our team's studies thus far have demonstrated, the stellar metallicity gradient measurements enabled by HST Ca H and K imaging can provide additional constraining power for various gradient formation mechanisms. On the theoretical side, detailed studies of metallicity gradients in high-fidelity simulations of dwarf galaxies, particularly in the UFD class, will be necessary for refining the interpretive lenses to bring to these observations.

6. Summary

In this paper we present the first well-sampled MDFs for And XVI ($L = 10^{4.9}\,L_\odot$) and And XXVIII ($L = 10^{5.5}\,L_\odot$) based on individual stellar metallicities measured using HST Ca H and K narrowband imaging. With a single HST pointing in each galaxy, we measure stellar metallicities with sample sizes and to precisions that ground-based Keck/DEIMOS spectroscopy has been able to attain only in M31 satellite galaxies that are hundreds or thousands of times brighter. We summarize the key results enabled by this novel data set:

1. From 95 stars in And XVI, we measure $\langle \text{[Fe/H]} \rangle = -2.17^{+0.05}_{-0.05}$, in good agreement with previous measurements from stacked stellar spectra. We also resolve $\sigma_{\text{[Fe/H]}} = 0.33^{+0.07}_{-0.07}$. Though its MDF is well described by a Gaussian statistically, visually it is also doubly peaked. We also measure a metallicity gradient ($\nabla_{\text{[Fe/H]}} = -0.23 \pm 0.15$ dex R_e^{-1}) at a significance of 1.5σ.

2. Compared to MW UFDs, with mean metallicities [Fe/H] ~ -2.6 (S. W. Fu et al. 2023), And XVI is more MR by ~ 0.5 dex. This property, alongside the putative double-peaked structure and the metallicity gradient, may result from its extended SFH, which is unusual among the currently known UFD population.

3. From 191 stars in And XXVIII, we measure $\langle \text{[Fe/H]} \rangle = -1.95^{+0.04}_{-0.04}$, $\sigma_{\text{[Fe/H]}} = 0.34^{+0.05}_{-0.05}$, and a strong metallicity gradient within $2R_e$: $\nabla_{\text{[Fe/H]}} = -0.46 \pm 0.10$ dex R_e^{-1}.

4. And XXVIII is more MR than And XVI despite its shorter SFH; these results affirm that stellar mass is a fundamental property setting the overall enrichment level of a galaxy (e.g., H. Lee et al. 2006; F. Calura et al. 2009; F. Mannucci et al. 2010; E. N. Kirby et al. 2013). With forthcoming chemical evolution studies, we will present a detailed characterization of the baryon cycle in galaxies of different masses with different SFHs.

5. The metallicity gradient measurements for these galaxies follow the age–gradient relation predicted in the FIRE-2 simulations (F. J. Mercado et al. 2021), as the observational consequence of gradients formed from the same stellar feedback hypothesized to form dark matter cores at the center of dwarf galaxy halos (G. S. Stinson et al. 2007; K. El-Badry et al. 2016).

As the only other current galactic ecosystem for which we can conduct resolved stellar population studies, M31 and its satellite system offer a necessary comparison point to the MW and its satellites. In particular, their study is critical to ongoing efforts to understand the impact of environment on dwarf galaxy evolution, the extent to which reionization has a universal impact on low-mass halos, and imprints of star formation baryonic feedback processes that can reconfigure luminous and dark matter within a galaxy. As our team has demonstrated in this paper and elsewhere, photometric

metallicity techniques are an efficient way to obtain detailed pictures of stellar metallicities in distant galaxies and will be highly complementary with future resolved stellar spectroscopy campaigns with JWST and ELT in the coming years.

Appendix
Table of Metallicity Measurements

In this appendix, we present Table 3, which contains all of the individual stellar metallicity measurements for And XVI and And XXVIII. In Table 4, we present all of the EMP star candidates in the two galaxies.

Table 3
Individual Stellar Metallicities

Galaxy	Star	R.A.	Decl.	F814W	F475W	F395N	VI	Ca H and K	[Fe/H]	Notes
AndXVI	0	14.883476	32.381190	20.064 ± 0.001	22.175 ± 0.002	24.056 ± 0.037	2.111 ± 0.002	-1.286 ± 0.037	$-1.77^{+0.10}_{-0.10} \pm 0.2$ (syst.)	Constrained
AndXVI	1	14.880947	32.381578	20.291 ± 0.001	22.333 ± 0.002	23.929 ± 0.034	2.042 ± 0.002	-1.467 ± 0.034	$-2.19^{+0.08}_{-0.07} \pm 0.2$ (syst.)	Constrained
AndXVI	2	14.877938	32.376751	20.332 ± 0.001	22.289 ± 0.002	23.719 ± 0.034	1.957 ± 0.002	-1.506 ± 0.034	$-2.41^{+0.09}_{-0.08} \pm 0.2$ (syst.)	Constrained
AndXVI	3	14.858829	32.384565	20.414 ± 0.001	22.381 ± 0.002	23.713 ± 0.024	1.967 ± 0.002	-1.618 ± 0.024	<-2.43	Ulim
AndXVI	4	14.894606	32.384091	20.487 ± 0.001	22.420 ± 0.002	23.788 ± 0.032	1.933 ± 0.002	-1.532 ± 0.032	$-2.46^{+0.10}_{-0.05} \pm 0.2$ (syst.)	Constrained
AndXVI	5	14.898027	32.374751	20.652 ± 0.001	22.532 ± 0.002	23.963 ± 0.034	1.880 ± 0.002	-1.389 ± 0.034	$-2.13^{+0.14}_{-0.16} \pm 0.2$ (syst.)	Constrained
AndXVI	6	14.872155	32.388600	20.995 ± 0.001	22.788 ± 0.003	24.059 ± 0.037	1.793 ± 0.003	-1.418 ± 0.037	$-2.33^{+0.17}_{-0.25} \pm 0.2$ (syst.)	Constrained
AndXVI	7	14.878955	32.384221	21.030 ± 0.002	22.831 ± 0.003	24.135 ± 0.035	1.801 ± 0.004	-1.397 ± 0.035	$-2.21^{+0.13}_{-0.26} \pm 0.2$ (syst.)	Constrained
AndXVI	9	14.906816	32.380212	21.117 ± 0.002	22.860 ± 0.003	24.134 ± 0.031	1.743 ± 0.004	-1.340 ± 0.031	$-2.07^{+0.14}_{-0.13} \pm 0.2$ (syst.)	Constrained
AndXVI	10	14.864351	32.377186	21.269 ± 0.002	23.013 ± 0.003	24.206 ± 0.036	1.744 ± 0.004	-1.423 ± 0.036	$-2.37^{+0.19}_{-0.25} \pm 0.2$ (syst.)	Constrained

Note. Measurements for all of the stars analyzed in this work.

(This table is available in its entirety in machine-readable form in the online article.)

**Table 4**
Candidate EMP Stars

Galaxy	Star	R.A.	Decl.	F814W	F475W	F395N	VI	Ca H and K	[Fe/H]
AndXVI	26	14.867180	32.379153	21.573 ± 0.002	23.239 ± 0.004	24.155 ± 0.034	1.666 ± 0.004	-1.583 ± 0.034	$-3.41^{+0.33}_{-0.39} \pm 0.5$ (syst.)
AndXVI	30	14.879237	32.388930	21.763 ± 0.002	23.419 ± 0.003	24.400 ± 0.040	1.656 ± 0.004	-1.503 ± 0.040	$-3.05^{+0.41}_{-0.32} \pm 0.5$ (syst.)
AndXVI	37	14.864885	32.388081	22.062 ± 0.003	23.684 ± 0.004	24.633 ± 0.044	1.622 ± 0.005	-1.484 ± 0.044	$-3.09^{+0.33}_{-0.41} \pm 0.5$ (syst.)
AndXVI	50	14.864719	32.378416	22.399 ± 0.003	23.935 ± 0.005	24.800 ± 0.051	1.536 ± 0.006	-1.439 ± 0.051	$-3.05^{+0.51}_{-0.51} \pm 0.5$ (syst.)
AndXVI	80	14.863572	32.377904	22.892 ± 0.004	24.352 ± 0.006	25.143 ± 0.067	1.460 ± 0.007	-1.399 ± 0.067	$-3.08^{+0.58}_{-0.58} \pm 0.5$ (syst.)
AndXVI	89	14.909581	32.370058	23.232 ± 0.005	24.659 ± 0.006	25.435 ± 0.067	1.427 ± 0.008	-1.364 ± 0.067	$-3.10^{+0.59}_{-0.59} \pm 0.5$ (syst.)
AndXVI	90	14.864426	32.384401	23.271 ± 0.006	24.698 ± 0.010	25.470 ± 0.076	1.427 ± 0.012	-1.369 ± 0.077	$-3.16^{+0.62}_{-0.54} \pm 0.5$ (syst.)
AndXXVIII	4	338.177742	31.228019	20.673 ± 0.001	22.960 ± 0.003	24.602 ± 0.043	2.287 ± 0.003	-1.789 ± 0.043	<-4.00
AndXXVIII	21	338.151042	31.219175	21.171 ± 0.001	23.229 ± 0.002	24.681 ± 0.047	2.058 ± 0.002	-1.635 ± 0.047	<-4.00
AndXXVIII	50	338.186547	31.203947	21.456 ± 0.002	23.386 ± 0.003	24.586 ± 0.044	1.930 ± 0.004	-1.695 ± 0.044	<-4.00
AndXXVIII	51	338.159931	31.215765	21.477 ± 0.001	23.416 ± 0.003	24.721 ± 0.056	1.939 ± 0.003	-1.604 ± 0.056	<-4.00
AndXXVIII	119	338.153888	31.224333	22.311 ± 0.002	24.045 ± 0.004	24.995 ± 0.048	1.734 ± 0.004	-1.651 ± 0.048	$-3.50^{+0.38}_{-0.23} \pm 0.5$ (syst.)
AndXXVIII	129	338.172690	31.217700	22.487 ± 0.003	24.144 ± 0.005	25.132 ± 0.088	1.657 ± 0.006	-1.497 ± 0.088	$-3.17^{+0.48}_{-0.48} \pm 0.5$ (syst.)
AndXXVIII	134	338.155764	31.225169	22.452 ± 0.002	24.150 ± 0.005	25.218 ± 0.056	1.698 ± 0.005	-1.479 ± 0.056	$-3.18^{+0.48}_{-0.47} \pm 0.5$ (syst.)
AndXXVIII	145	338.185173	31.188016	22.636 ± 0.003	24.322 ± 0.005	25.314 ± 0.074	1.686 ± 0.006	-1.537 ± 0.074	$-3.47^{+0.52}_{-0.36} \pm 0.5$ (syst.)
AndXXVIII	157	338.189276	31.199485	22.746 ± 0.003	24.316 ± 0.005	25.221 ± 0.066	1.570 ± 0.006	-1.450 ± 0.066	$-3.11^{+0.48}_{-0.47} \pm 0.5$ (syst.)
AndXXVIII	174	338.142529	31.212665	23.016 ± 0.004	24.598 ± 0.006	25.506 ± 0.073	1.582 ± 0.007	-1.465 ± 0.073	$-3.32^{+0.56}_{-0.46} \pm 0.5$ (syst.)
AndXXVIII	192	338.151661	31.218511	23.380 ± 0.004	24.867 ± 0.006	25.770 ± 0.098	1.487 ± 0.007	-1.328 ± 0.098	$-3.05^{+0.62}_{-0.61} \pm 0.5$ (syst.)
AndXXVIII	196	338.148343	31.212334	23.508 ± 0.005	25.083 ± 0.008	26.033 ± 0.101	1.575 ± 0.009	-1.412 ± 0.101	$-3.26^{+0.47}_{-0.49} \pm 0.5$ (syst.)

Note. All of our identified EMP candidates in And XVI and And XXVIII.

(This table is available in machine-readable form in the online article.)

ORCID iDs

Sal Wanying Fu ⓘ https://orcid.org/0000-0003-2990-0830
Daniel R. Weisz ⓘ https://orcid.org/0000-0002-6442-6030
Nicolas Martin ⓘ https://orcid.org/0000-0002-1349-202X
Michelle L. M. Collins ⓘ https://orcid.org/0000-0002-1693-3265
Alessandro Savino ⓘ https://orcid.org/0000-0002-1445-4877
Michael Boylan-Kolchin ⓘ https://orcid.org/0000-0002-9604-343X
Patrick Côté ⓘ https://orcid.org/0000-0003-1184-8114
Mario L. Mateo ⓘ https://orcid.org/0000-0002-3856-232X
Francisco J. Mercado ⓘ https://orcid.org/0000-0002-5908-737X
Nathan R. Sandford ⓘ https://orcid.org/0000-0002-7393-3595
Evan D. Skillman ⓘ https://orcid.org/0000-0003-0605-8732

References

Amorisco, N. C. 2017, ApJ, 844, 64
Andrews, B. H., Weinberg, D. H., Schönrich, R., & Johnson, J. A. 2017, ApJ, 835, 224
Azartash-Namin, B., Engelhardt, A., Munshi, F., et al. 2024, ApJ, 970, 40
Battaglia, G., Taibi, S., Thomas, G. F., & Fritz, T. K. 2022, A&A, 657, A54
Battaglia, G., Tolstoy, E., Helmi, A., et al. 2006, A&A, 459, 423
Bechtol, K., Drlica-Wagner, A., Balbinot, E., et al. 2015, ApJ, 807, 50
Beers, T. C., Preston, G. W., & Shectman, S. A. 1985, AJ, 90, 2089
Belokurov, V., Zucker, D. B., Evans, N. W., et al. 2007, ApJ, 654, 897
Benítez-Llambay, A., Navarro, J. F., Abadi, M. G., et al. 2016, MNRAS, 456, 1185
Bennet, P., Patel, E., Sohn, S. T., et al. 2024, ApJ, 971, 23, arXiv:2312.09276
Brasseur, C. M., Martin, N. F., Macciò, A. V., Rix, H.-W., & Kang, X. 2011, ApJ, 743, 179
Brown, T. M., Tumlinson, J., Geha, M., et al. 2014, ApJ, 796, 91
Bullock, J. S., & Boylan-Kolchin, M. 2017, ARA&A, 55, 343
Calura, F., Pipino, A., Chiappini, C., Matteucci, F., & Maiolino, R. 2009, A&A, 504, 373
Carrera, R., Pancino, E., Gallart, C., & del Pino, A. 2013, MNRAS, 434, 1681
Chiti, A., Frebel, A., Mardini, M. K., et al. 2021a, ApJS, 254, 31
Chiti, A., Frebel, A., Simon, J. D., et al. 2021b, NatAs, 5, 392
Choi, J., Dotter, A., Conroy, C., et al. 2016, ApJ, 823, 102
Collins, M. L. M., Chapman, S. C., Rich, R. M., et al. 2013, ApJ, 768, 172
Collins, M. L. M., Chapman, S. C., Rich, R. M., et al. 2014, ApJ, 783, 7
Collins, M. L. M., Martin, N. F., Rich, R. M., et al. 2015, ApJL, 799, L13
Crnojević, D., Sand, D. J., Zaritsky, D., et al. 2016, ApJL, 824, L14
Doliva-Dolinsky, A., Martin, N. F., Thomas, G. F., et al. 2022, ApJ, 933, 135
Doliva-Dolinsky, A., Martin, N. F., Yuan, Z., et al. 2023, ApJ, 952, 72
Dolphin, A., 2016 DOLPHOT: Stellar Photometry, ascl:1608.013
Dolphin, A. E. 2000, PASP, 112, 1383
Dotter, A. 2016, ApJS, 222, 8
Drlica-Wagner, A., Bechtol, K., Rykoff, E. S., et al. 2015, ApJ, 813, 109
El-Badry, K., Wetzel, A., Geha, M., et al. 2016, ApJ, 820, 131
Errani, R., Navarro, J. F., Ibata, R., & Penarrubia, J. 2022, MNRAS, 511, 6001
Foreman-Mackey, D., Hogg, D. W., Lang, D., & Goodman, J. 2013, PASP, 125, 306
Fu, S. W., Weisz, D. R., Starkenburg, E., et al. 2022, ApJ, 925, 6
Fu, S. W., Weisz, D. R., Starkenburg, E., et al. 2023, ApJ, 958, 23, arXiv:2306.06260
Fu, S. W., Weisz, D. R., Starkenburg, E., et al. 2024, ApJ, 965, 36
Gallart, C., Monelli, M., Mayer, L., et al. 2015, ApJL, 811, L18
Gallart, C., Monelli, M., Ruiz-Lara, T., et al. 2021, ApJ, 909, 192
Garrison-Kimmel, S., Rocha, M., Boylan-Kolchin, M., Bullock, J. S., & Lally, J. 2013, MNRAS, 433, 3539
Geha, M., Weisz, D., Grocholski, A., et al. 2015, ApJ, 811, 114
Gelman, A., & Rubin, D. B. 1992, StaSc, 7, 457
Governato, F., Brook, C., Mayer, L., et al. 2010, Natur, 463, 203
Grevesse, N., & Sauval, A. J. 1998, SSRv, 85, 161
Hausammann, L., Revaz, Y., & Jablonka, P. 2019, A&A, 624, A11
Ho, N., Geha, M., Munoz, R. R., et al. 2012, ApJ, 758, 124
Ho, N., Geha, M., Tollerud, E. J., et al. 2015, ApJ, 798, 77
Hogg, D. W., Bovy, J., & Lang, D. 2010, arXiv:1008.4686
Homma, D., Chiba, M., Komiyama, Y., et al. 2019, PASJ, 71, 94
Ibata, R., Martin, N. F., Irwin, M., et al. 2007, ApJ, 671, 1591

Jones, M. G., Mutlu-Pakdil, B., Sand, D. J., et al. 2023, ApJL, 957, L5
Kacharov, N., Battaglia, G., Rejkuba, M., et al. 2017, MNRAS, 466, 2006
Kirby, E. N., Cohen, J. G., Guhathakurta, P., et al. 2013, ApJ, 779, 102
Kirby, E. N., Gilbert, K. M., Escala, I., et al. 2020, AJ, 159, 46
Kvasova, K., Kirby, E. N., & Beaton, R. L. 2024, ApJ, 972, 19, arXiv:2404.11804
Laevens, B. P. M., Martin, N. F., Bernard, E. J., et al. 2015, ApJ, 813, 44
Lee, H., Skillman, E. D., Cannon, J. M., et al. 2006, ApJ, 647, 970
Letarte, B., Chapman, S. C., Collins, M., et al. 2009, MNRAS, 400, 1472
Li, T. S., Simon, J. D., Drlica-Wagner, A., et al. 2017, ApJ, 838, 8
Longeard, N., Jablonka, P., Battaglia, G., et al. 2023, MNRAS, 525, 3086
Madau, P., Shen, S., & Governato, F. 2014, ApJL, 789, L17
Mannucci, F., Cresci, G., Maiolino, R., Marconi, A., & Gnerucci, A. 2010, MNRAS, 408, 2115
Marcolini, A., D'Ercole, A., Battaglia, G., & Gibson, B. K. 2008, MNRAS, 386, 2173
Martin, N. F., Chambers, K. C., Collins, M. L. M., et al. 2014, ApJL, 793, L14
Martin, N. F., Ibata, R. A., Lewis, G. F., et al. 2016, ApJ, 833, 167
Martin, N. F., Ibata, R. A., McConnachie, A. W., et al. 2013, ApJ, 776, 80
Martin, N. F., Starkenburg, E., Yuan, Z., et al. 2023, arXiv:2308.01344
Martínez-Vázquez, C. E., Monelli, M., Cassisi, S., et al. 2021, MNRAS, 508, 1064
McConnachie, A. W., Huxor, A., Martin, N. F., et al. 2008, ApJ, 688, 1009
McConnachie, A. W., & Irwin, M. J. 2006a, MNRAS, 365, 902
McConnachie, A. W., & Irwin, M. J. 2006b, MNRAS, 365, 1263
McQuinn, K. B. W., Skillman, E. D., Dolphin, A., et al. 2015, ApJ, 812, 158
Mercado, F. J., Bullock, J. S., Boylan-Kolchin, M., et al. 2021, MNRAS, 501, 5121
Monelli, M., Martínez-Vázquez, C. E., Bernard, E. J., et al. 2016, ApJ, 819, 147
Munshi, F., Brooks, A. M., Applebaum, E., et al. 2021, ApJ, 923, 35
Navarro, J. F., Eke, V. R., & Frenk, C. S. 1996, MNRAS, 283, L72
Ou, X., Chiti, A., Shipp, N., et al. 2024, ApJ, 966, 33
Pace, A. B., Erkal, D., & Li, T. S. 2022, ApJ, 940, 136
Pace, A. B., Kaplinghat, M., Kirby, E., et al. 2020, MNRAS, 495, 3022
Patel, E., Kallivayalil, N., Garavito-Camargo, N., et al. 2020, ApJ, 893, 121
Peñarrubia, J., Navarro, J. F., & McConnachie, A. W. 2008, ApJ, 673, 226
Revaz, Y., & Jablonka, P. 2018, A&A, 616, A96
Sacchi, E., Richstein, H., Kallivayalil, N., et al. 2021, ApJL, 920, L19
Sales, L. V., Helmi, A., Battaglia, G., & Kravtsov, A. V. 2010, AdAst, 2010, 194345
Sand, D. J., Mutlu-Pakdil, B., Jones, M. G., et al. 2022, ApJL, 935, L17
Sandford, N. R., Weinberg, D. H., Weisz, D. R., & Fu, S. W. 2024, MNRAS, 530, 2315
Savino, A., Weisz, D. R., Skillman, E. D., et al. 2022, ApJ, 938, 101
Savino, A., Weisz, D. R., Skillman, E. D., et al. 2023, ApJ, 956, 86
Schlafly, E. F., & Finkbeiner, D. P. 2011, ApJ, 737, 103
Schroyen, J., De Rijcke, S., Koleva, M., Cloet-Osselaer, A., & Vandenbroucke, B. 2013, MNRAS, 434, 888
Simon, J. D. 2019, ARA&A, 57, 375
Simon, J. D., Brown, T. M., Drlica-Wagner, A., et al. 2021, ApJ, 908, 18
Simon, J. D., Brown, T. M., Mutlu-Pakdil, B., et al. 2023, ApJ, 944, 43
Skillman, E. D., Monelli, M., Weisz, D. R., et al. 2017, ApJ, 837, 102
Slater, C. T., Bell, E. F., & Martin, N. F. 2011, ApJL, 742, L14
Slater, C. T., Bell, E. F., Martin, N. F., Tollerud, E. J., & Ho, N. 2015, ApJ, 806, 230
Starkenburg, E., Hill, V., Tolstoy, E., et al. 2010, A&A, 513, A34
Starkenburg, E., Hill, V., Tolstoy, E., et al. 2013, A&A, 549, A88
Starkenburg, E., Martin, N., Youakim, K., et al. 2017, MNRAS, 471, 2587
Stinson, G. S., Dalcanton, J. J., Quinn, T., Kaufmann, T., & Wadsley, J. 2007, ApJ, 667, 170
Strömgren, B. 1966, ARA&A, 4, 433
Taibi, S., Battaglia, G., Leaman, R., et al. 2022, A&A, 665, A92
Tau, E. A., Vivas, A. K., & Martínez-Vázquez, C. E. 2024, AJ, 167, 57
Tolstoy, E., Hill, V., & Tosi, M. 2009, ARA&A, 47, 371
Vanhollebeke, E., Groenewegen, M. A. T., & Girardi, L. 2009, A&A, 498, 95
Vargas, L. C., Geha, M. C., & Tollerud, E. J. 2014, ApJ, 790, 73
Walker, M. G., Mateo, M., Olszewski, E. W., et al. 2009, ApJ, 704, 1274
Waller, F., Venn, K. A., Sestito, F., et al. 2023, MNRAS, 519, 1349
Weinberg, D. H., Andrews, B. H., & Freudenburg, J. 2017, ApJ, 837, 183
Weisz, D. R., Dolphin, A. E., Skillman, E. D., et al. 2014a, ApJ, 789, 147
Weisz, D. R., Savino, A., & Dolphin, A. E. 2023, ApJ, 948, 50
Weisz, D. R., Skillman, E. D., Hidalgo, S. L., et al. 2014b, ApJ, 789, 24